Molecular Dynamics Simulations of the Elastic Moduli of Polymer-Carbon Nanotube Composites

Michael Griebel and Jan Hamaekers

Department of Applied Mathematics,
Division of Scientific Computing and Numerical Simulation,
University of Bonn, Germany

Abstract

The elastic moduli of polymer-carbon nanotube composites are examined by molecular dynamics simulations of a single-walled carbon nanotube embedded in polyethylene. The overall system is modeled with a many-body bond order potential due to Brenner. Alternatively, only the carbon nanotube is modeled with Brenner's potential and the polyethylene matrix is modeled by a united-atom potential. For these systems we perform molecular dynamics simulations to derive stress-strain curves. Here, we use the Parrinello-Rahman approach to apply external stress to a periodic system. To compare the elastic moduli of the composite with rule-of-mixtures predictions, we study three periodic systems, an infinite carbon nanotube, a finite carbon nanotube embedded in polyethylene and the polyethylene matrix itself. The results show an excellent agreement with the macroscopic rule-of-mixtures in the case of the very long nanotube and with an extended rule-of-mixtures in the case of the short nanotube.

Key words: molecular dynamics simulation, NPT ensemble, polymer-carbon nanotube composites, elastic moduli.
PACS: 02.70.Ns, 61.48.+c, 62.20.Dc, 62.25.+g, 81.05.Qk, 81.05.Tp, 83.10.Rs.

Email addresses: griebel@iam.uni-bonn.de (Michael Griebel), hamaeker@iam.uni-bonn.de (Jan Hamaekers).
URLs: http://wissrech.iam.uni-bonn.de/people/griebel.html (Michael Griebel), http://wissrech.iam.uni-bonn.de/people/hamaekers.html (Jan Hamaekers).

1 Introduction

With the discovery of pure carbon structures different from graphite and diamond, a new fast developing area in nanomaterial science started recently [1]. In particular, very long tube-like structures were first reported by Iijima in 1991; see [2]. The diameter range of these carbon nanotubes is in the nanometer range and their length can be in the micrometer range [3]. Due to their structure and form, they seem to tolerate extreme distortion without fracture. They also show elastic bending, twisting, buckling and other reversible deformations. The bending stiffness is in the range of 0.4 to 4 TPa [4]; furthermore a local tension of hundreds of Giga Pascal can be reached before fracture occurs [5]. Due to their properties carbon nanotubes can be used to reinforce polymer composites. Here, they possess the potential for large increases in strength and stiffness when compared to typical carbon-fiber-reinforced polymer composites. Therefore, nanotube-polymer composites have gained considerable interest in the materials research community.

Meanwhile, some nanotube composite materials have been characterized experimentally [6–15]. This however is a demanding and expensive task. To this end, computational methods can be used to greatly facilitate the development of nanotube composite materials. Computer simulations allow for parametric studies of the influence of composite and geometry on the material properties. In particular, *first-principle* techniques [16–19], *semi-empirical* schemes [20], and *empirical potential* methods [16,17,21–27] have been applied successfully to study nanostructures. Here, especially for large systems with hundred atoms and more, molecular dynamics simulations are an important tool to better understand the properties of polymer-carbon nanotube composites. In this work, we derive stress-strain curves from molecular dynamics simulations of polymer-carbon nanotube composites to predict their macroscopic elastic moduli and compare them to a *rule-of-mixtures*, which takes only the volume fraction of the fiber into account, and an *extented rule-of-mixtures*, which takes also the distribution of the fiber into account [28,29]. Here, we use empirical potentials because of the size of the systems we study.

In several earlier works, molecular dynamics simulations have been successfully applied to predict elastic properties of polymer-carbon nanotube composites [30–32]. Here, the application of strain has been accomplished by uniformly expanding the length of the simulation cell in the direction of the deformation. To equilibrate the system for the new cell size, the coordinates of the atoms are re-scaled to fit to the new geometry, and a molecular dynamics simulation or a potential energy minimization is performed. This way, the stress at different strain values can be calculated successively. Among this static technique [33,16,21,23,20,26,27,34], there exist two methods based on the Parrinello-Rahman [35] approach. First, the fluctuation method to

calculate the elastic constants [36–42,34], and second the dynamic method. The dynamic method involves using constant stress molecular dynamics to measure the stress-strain behavior of a material subjected to an applied load [43,44,39,45,46]. In the present work, we carry out the application of strain by employing a Parrinello-Rahman-Nosé Lagrangian to control stress and temperature in an NPT ensemble [35,47]. Similar to the dynamic method we apply an external stress tensor within the equations of motion and measure the linear stress tensor. We compute the stress-strain curves of three periodic model systems, an infinite $(10, 10)$ single-walled carbon nanotube, a finite $(10, 10)$ single-walled capped carbon nanotube embedded in polyethylene, and the polyethylene matrix itself. To model the bonded interaction within these hydrocarbon systems, we use a many-body bond order potential due to Brenner [48,49]. Alternatively, we model the polyethylene matrix by a united-atom potential [50] and just the carbon nanotube by Brenner's potential. In both models, the nonbonded interaction of the atoms is represented by a simple Lennard-Jones potential. We exploit the slopes of the stress-strain curves to derive different elastic moduli and constants.

The remainder of this paper is organized as follows: In section 2 we give the computational methods which we used in our study of polymer-carbon nanotube composites. Here, in section 2.1 we give the details of the the molecular dynamics approach in the framework of an NPT ensemble. In section 2.2 we discuss the two different models which we use to represent hydrocarbon systems. In section 2.3 we present a computational method to derive the *elasticity tensor*. Section 3 gives the results of our numerical experiments. We relate these results to the two different rule-of-mixtures in section 4. Finally we give some concluding remarks.

2 Computational Methods

In this section we describe the modeling and implementational aspects of our approach. First we discuss isobaric-isothermal molecular dynamics simulations due to Parrinello-Rahman. Then we give a review on the potentials we use to model hydrocarbon systems. Finally we discuss the generation of stress-strain curves and the computation of elastic moduli and constants.

NPT ensemble

The Hamiltonian for a molecular system with N particles, constant volume and constant energy is given by

$$\mathcal{H} = \frac{1}{2}\sum_{i=1}^{N}\frac{\vec{p}_{\vec{x}_i}^{T}\vec{p}_{\vec{x}_i}}{m_i} + V(\vec{x}_1,\ldots,\vec{x}_N) \tag{1}$$

with cartesian coordinates $\vec{x}_i$, moments $\vec{p}_{\vec{x}_i}$, masses m_i and a conservative potential V. The corresponding ensemble is called NVE. To obtain an isothermal-isobaric ensemble, or NPT ensemble which allows to control pressure and temperature, we introduce additional degrees of freedom. To this end, we define a 3×3 matrix $\hat{h} = [\vec{a}_1, \vec{a}_2, \vec{a}_3]$ and re-scale the coordinates $\hat{\vec{s}}_i = \hat{h}^{-1}\vec{x}_i$. Here, $\vec{a}_1, \vec{a}_2, \vec{a}_3$ are the basis vectors of the simulation cell with volume $\Omega = \det\hat{h} > 0$. We also re-scale the time t by $\bar{t} = \int_0^t \gamma(\tau)d\tau$ and obtain the velocities in the form $\dot{\vec{x}}_i(\bar{t}) = \gamma\hat{h}\dot{\hat{\vec{s}}}_i(t)$. Furthermore, we define a fictitious potential $P_{\text{ext}}\det\hat{h}$ with the externally applied pressure P_{ext} and a fictitious potential $N_f k_B T\ln\gamma$, where T denotes the target temperature, N_f denotes the number N_f of degrees of freedom of the system, and k_B is Boltzmann's constant. This way we have nine additional degrees of freedom h_{ij} for the pressure control and one degree of freedom for the temperature control. Now a so-called Parrinello-Rahman-Nosé Lagrangian can be postulated and an extended Hamiltonian

$$\mathcal{H} = \frac{1}{2}\sum_{i=1}^{N}\frac{\vec{p}_{\vec{s}_i}^{T}G\vec{p}_{\vec{s}_i}}{m_i} + \frac{1}{2}\frac{\operatorname{tr}(p_h^T p_h)}{M_P} + \frac{1}{2}\frac{p_\gamma^2}{M_T} + V + P_{\text{ext}}\det h + N_f k_B T\eta \tag{2}$$

with variables

$$\vec{s}_i(t) := \hat{\vec{s}}_i(\bar{t}), \quad h(t) := \hat{h}(\bar{t}), \quad G := h^T h, \quad \eta(t) := \ln\gamma(\bar{t})\,,$$

can be derived [35,47,51]. Here, M_P is a fictitious mass or inertia parameter to control the time-scale of motion of the cell h, and M_T is an analogous parameter with respect to temperature. The resulting equations of motion then read

$$\dot{\vec{s}}_i = \frac{\vec{p}_{\vec{s}_i}}{m_i}, \quad \dot{h} = \frac{p_h}{M_P}, \quad \dot{\eta} = \frac{p_\gamma}{M_T}\,, \tag{3}$$

$$\dot{\vec{p}}_{\vec{s}_i} = h^{-1}\vec{F}_i - G^{-1}\dot{G}p_{\vec{s}_i} - \frac{p_\gamma}{M_T}p_{\vec{s}_i}\,, \tag{4}$$

$$\dot{p}_h = \left(\Pi_{\text{int}} - \operatorname{diag}\left(P_{\text{ext}}\right)\right)h^{-T}\det h - \frac{p_\gamma}{M_T}p_h\,, \tag{5}$$

$$\dot{p}_\gamma = \sum_{i=1}^{N}\frac{\vec{p}_{\vec{s}_i}^{T}G\vec{p}_{\vec{s}_i}}{m_i} + \frac{\operatorname{tr}(p_h^T p_h)}{M_P} - N_f k_B T\,, \tag{6}$$

where $\vec{F}_i := -\nabla_{\vec{x}_i} V$ denotes the force which is contributed by the potential V and acts on particle i. Furthermore, the internal stress tensor Π_{int} can be written as

$$\begin{aligned} \Pi_{\text{int}} = \frac{1}{\det h} \sum_{i=1}^{N} m_i h \vec{s}_i \vec{s}_i^T h^T + \Pi_{\text{int}}^{\text{pot}}, \quad \Pi_{\text{int}}^{\text{pot}} = \frac{1}{\det h} F_h h^T, \\ (F_h)_{\alpha\beta} := -\frac{d}{d\, h_{\alpha\beta}} V, \quad \alpha, \beta \in \{1,2,3\}. \end{aligned} \tag{7}$$

In particular, one third of the trace of the internal stress tensor equals the instantaneous internal pressure $P_{\text{int}} = \frac{1}{3}\text{tr}(\Pi_{\text{int}})$. If we assume that the potential V does not depend explicitly on the cell matrix h, the 3×3 matrix $F_h = -\frac{d}{dh} V(h\vec{s}_1, \ldots, h\vec{s}_N)$ can be written as $F_h = \sum_{i=1}^{N} \vec{F}_i \vec{s}_i^T$ by exploiting the chain rule. We calculate the instantaneous temperature

$$T_{\text{instan}} = \frac{2E_{\text{kin}}}{N_f k_B}, \quad E_{\text{kin}} = \frac{1}{2} \sum_{i=1}^{N} \frac{\vec{p}_{s_i}^T G \vec{p}_{\vec{s}_i}}{m_i}$$

as usual; the thermodynamic temperature is the time-average of T_{instan}.

Periodic systems

If periodic boundary conditions are used, the potential V depends explicitly on the matrix h, because atoms in the unit cell interact not only with other atoms in the same unit cell but also with their translated images. These interactions with the images must be included correctly in the potential contribution expressions $\Pi_{\text{int}}^{\text{pot}}$ and $\vec{F}_i$. In the case of a potential $V(\vec{x}_1, \ldots, \vec{x}_N) = \sum_{i<j} v_{\text{pair}}(r_{ij})$ which only involves pair terms $v_{\text{pair}}(r_{ij})$, where $\vec{r}_{ij} := \vec{x}_j - \vec{x}_i$ and $r_{ij} := \|\vec{r}_{ij}\|$, the periodic potential can be written as

$$V^{\text{periodic}}(h, \vec{x}_1, \ldots, \vec{x}_N) = \sum_{i<j} v_{\text{pair}}(r_{ij}) + \sum_{i \neq j} \sum_{\underline{s} \in \mathbb{Z}^3 \setminus (0,0,0)} v_{\text{pair}}(r_{ij,h\underline{s}}), \tag{8}$$

where $r_{ij,h\underline{s}} := \|\vec{r}_{ij,h\underline{s}}\|$ and $\vec{r}_{ij,h\underline{s}} := \vec{x}_j + h\underline{s} - \vec{x}_i$. Note that the infinite series in equation (8) is usually convergent, because the pair terms are of short range. If we define pair forces $\vec{F}_{ij} := -\frac{d}{d\vec{x}_i} v_{\text{pair}}(r_{ij})$, we evaluate the potential contribution to the forces on the particles in equation (4) in the form

$$\vec{F}_i = \sum_{j \neq i} \vec{F}_{ij} + \sum_{j} \sum_{\underline{s} \in \mathbb{Z}^3 \setminus (0,0,0)} \vec{F}_{ij,h\underline{s}},$$

with $\vec{F}_{ij,h\underline{s}} := \frac{d}{d\vec{x}_i} v_{\text{pair}}(r_{ij,h\underline{s}})$. Furthermore, we can exploit Newton's third law $\vec{F}_{ij} = -\vec{F}_{ji}$ and the corresponding relation $\vec{F}_{ij}\vec{r}_i^T + \vec{F}_{ji}\vec{r}_j^T = -\vec{F}_{ij}\vec{r}_{ij}$ to write

the potential contribution of the internal stress tensor in equation (7) as

$$\Pi_{\text{int}}^{\text{pot}} = \frac{1}{\det h}\left(\sum_{i<j} -\vec{F}_{ij}\vec{r}_{ij}^{T} + \sum_{i\neq j}\sum_{\underline{s}\in\mathbb{Z}^3\setminus(0,0,0)} -\vec{F}_{ij,h\underline{s}}\vec{r}_{ij,h\underline{s}}^{T}\right).$$

In a way similar to the pair-dependent terms $v_{\text{pair}}(r_{ij})$, we treat angle-dependent three-body terms $v_{\text{ang}}(\theta_{ijk})$ and torsional-dependent four-body terms $v_{\text{tor}}(\phi_{ijkl})$. Here, θ_{ijk} denotes the angle between $\vec{r}_{ij}$ and $\vec{r}_{ik}$ and ϕ_{ijkl} denotes the so-called torsional or dihedral angle $\sphericalangle(\vec{r}_{ij}\times\vec{r}_{jk}, \vec{r}_{jk}\times\vec{r}_{kl})$. Analogous to equation (8) and Newton's third law, we define the corresponding periodic potential and the force contribution $\vec{F}_n^{ijk} := -\frac{d}{d\vec{x}_n} v_{\text{ang}}(\theta_{ijk})$. We then exploit the relations

$$\begin{aligned} \vec{F}_i^{ijk} &= -\vec{F}_j^{ijk} - \vec{F}_k^{ijk}, \\ \vec{F}_i^{ijk}\vec{r}_i + \vec{F}_j^{ijk}\vec{r}_j + \vec{F}_k^{ijk}\vec{r}_k &= \vec{F}_j^{ijk}\vec{r}_{ij}^{T} + \vec{F}_k^{ijk}\vec{r}_{ik}^{T} \end{aligned}$$

to evaluate the corresponding potential contributions $\vec{F}_i$ and $\Pi_{\text{int}}^{\text{pot}}$ in the angle-dependent case. In the dihedral angle or torsional-dependent case, we define $\vec{F}_n^{ijkl} := -\frac{d}{d\vec{x}_n} v_{\text{tor}}(\phi_{ijkl})$ and use the relations

$$\begin{aligned} \vec{F}_i^{ijkl} &= -\vec{F}_j^{ijkl} - \vec{F}_k^{ijkl} - \vec{F}_l^{ijkl}, \\ \vec{F}_i^{ijkl}\vec{r}_i + \vec{F}_j^{ijkl}\vec{r}_j + \vec{F}_k^{ijkl}\vec{r}_k + \vec{F}_l^{ijkl}\vec{r}_l &= -\vec{F}_i^{ijkl}\vec{r}_{ij}^{T} - (\vec{F}_i^{ijkl} + \vec{F}_j^{ijkl})\vec{r}_{jk}^{T} + \vec{F}_l^{ijkl}\vec{r}_{kl}^{T}. \end{aligned}$$

In particular, the contribution of the torsional potential to the trace of the stress tensor is zero and therefore the contribution to the pressure is zero as well [52]. However, the contribution to the full stress tensor must be taken into account. Note that the internal stress tensor Π_{int} is symmetric in the case of pair, angle and torsional potentials.

Time integration

For the numerical solution of the system of the ordinary differential equations (3)-(6), we have to employ a time integration scheme. Here, the following problem appears: The forces in the equations of motion (3)-(6) are velocity-dependent. This usually presents a difficulty to "non-predictor-corrector" algorithms which are based on the assumption that the forces depend on the coordinates only. We therefore use the "predictor-corrector" scheme (9). It is

based on Beeman's approach [53] and was later modified by Refson [54]:

$$
\begin{aligned}
&\text{a)} \quad q(t+\Delta t) &&:= q(t) + \Delta t \tfrac{p_q(t)}{m} + \tfrac{\Delta t^2}{6m}\left[4\dot{p}_q(t) - \dot{p}_q(t-\Delta t)\right] \\
&\text{b)} \quad p_q^{(p)}(t+\Delta t) &&:= p_q(t) + \tfrac{\Delta t}{2}\left[3\dot{p}_q(t) - \dot{p}_q(t-\Delta t)\right] \\
&\text{c)} \quad \dot{p}_q(t+\Delta t) &&:= F\left(\{q_i(t+\Delta t), p_{q_i}^{(p)}(t+\Delta t)\}, i = 1 \ldots n\right) \\
&\text{d)} \quad p_q^{(c)}(t+\Delta t) &&:= p_q(t) + \tfrac{\Delta t}{6}\left[2\dot{p}_q(t+\Delta t) + 5\dot{p}_q(t) - \dot{p}_q(t-\Delta t)\right] \\
&\text{e) Replace } p_q^{(p)} \text{ with } p_q^{(c)} \text{ and goto c). Iterate to convergence.}
\end{aligned}
\tag{9}
$$

Here, the symbol q represents any dynamic variable (the scaled coordinates, the cell matrix or the variable of the thermostat) and $p_q^{(p)}$ and $p_q^{(c)}$ represent the "predicted" and "corrected" moments, respectively. The predictor-corrector cycle (steps c) to e)) is iterated until the predicted and corrected velocities have converged with respect to a relative precision. This iteration usually takes two or three cycles in practice. In particular, the expensive evaluation of the coordinate-dependent terms of the force calculation in step c) has to be performed just once per time step. Only the relatively cheap evaluation of the velocity-dependent terms of the force calculation has to be computed in every cycle.

Note that compared to the Hamiltonian (1) of an NVE ensemble, the physical energy $E_{\text{kin}} + V$ contained in the Hamiltonian (2) of an NPT ensemble is not conserved. But the Hamiltonian (2) of the physical energy, the fictitious energy of the barostat and the fictitious energy of the thermostat remain constant over time.

2.2 Potentials for Hydrocarbons

Atomistic model (Model I)

To represent hydrocarbon systems (i.e. the carbon nanotube and the polyethylene matrix) we use a so-called atomistic model in which all the atoms in the monomeric units are treated explicitly. To model the short-range chemical interactions, we employ Brenner's potential, which is a reactive empirical potential for hydrocarbons involving bond order terms (REBO). It describes covalent bonding within both the polymer and the carbon nanotubes [48]. Additionally we use a Lennard-Jones potential to characterize nonbonded van der Waals interactions [55,56]. The resulting potential is given as a sum over bonds

$$
E_{\text{pot}} = \sum_i \sum_{i<j} \left(V_R(r_{ij}) - \bar{B}_{ij} V_A(r_{ij}) + V_W(r_{ij}) \right) , \tag{10}
$$

where $r_{ij} = |\vec{x}_j - \vec{x}_i|$ denotes the distance between atoms i and j. Here, V_R is a pair-potential term to model the interatomic core-core repulsive interactions,

V_A is a pair-potential term to describe the attractive interactions due to the valence electrons. $\bar{B}_{ij}$ is a so called many-body empirical bond-order term which modulates valence electron densities and depends on the bond lengths and the angles. V_W denotes the contribution from the Lennard-Jones potential. It has in particular a support different from that of the short-range REBO potential.

The repulsive and the attractive pair terms V_R and V_A are derived from Morse potentials and are restricted to immediate neighbors or bonded atoms by a factor $f(r_{ij})$. This smoothed truncation function $f(r_{ij})$ reads as

$$f(r_{ij}) = \begin{cases} 1 & : \quad r_{ij} \leq R_{ij}^{(1)} \\ \frac{1}{2}\left[1 + \cos\left(\pi \frac{r_{ij} - R_{ij}^{(1)}}{R_{ij}^{(2)} - R_{ij}^{(1)}}\right)\right] & : \quad R_{ij}^{(1)} \leq r_{ij} \leq R_{ij}^{(2)} \\ 0 & : \quad r_{ij} \geq R_{ij}^{(2)} \end{cases},$$

where the cutoff parameters $R_{ij}^{(1)}$ and $R_{ij}^{(2)}$ only depend on the type of the atom i and j, i.e. they are dependent on whether i and j are carbon or hydrogen atoms. Furthermore, all terms which are used to evaluate the many-body empirical bond-order term $\bar{B}_{ij}$ are restricted to bonded atoms by the factor f as well. To define a continuously differentiable potential V_W for the contribution of the nonbonded interactions, we use cubic spline functions $S^{(1)}$ and $S^{(2)}$. Here, V_W reads

$$V_W(r_{ij}) = \begin{cases} 0 & : \quad r_{ij} \leq R_{ij}^{(2)} \\ S^{(1)}(r_{ij}) & : \quad R_{ij}^{(2)} \leq r_{ij} \leq R_{ij}^{(3)} \\ 4\epsilon_{ij}\left[(\sigma_{ij}/r_{ij})^{12} - (\sigma_{ij}/r_{ij})^{6}\right] & : \quad R_{ij}^{(3)} \leq r_{ij} \leq R_{ij}^{(4)} \\ S^{(2)}(r_{ij}) & : \quad R_{ij}^{(4)} \leq r_{ij} \leq R_{ij}^{(5)} \\ 0 & : \quad r_{ij} \geq R_{ij}^{(5)} \end{cases}$$

where the Lennard-Jones parameters ϵ_{ij} and σ_{ij} and the radii $R_{ij}^{(2)}$, $R_{ij}^{(3)}$, $R_{ij}^{(4)}$ and $R_{ij}^{(5)}$ are given in table 1. Note however that all the terms in potential (10) are restricted by the cutoff parameters $R_{ij}^{(2)}$ or $R_{ij}^{(5)}$. Thus, we can use the linked cell technique for an efficient implementation. A straightforward domain decomposition approach then allows for a parallel implementation. This results in a parallel complexity of the order $O(\rho^3 N/P)$ [24,51]. Especially, if the density ρ is assumed to be nearly constant, i.e. if the particles are more or less uniformly distributed, then the average complexity scales linearly with N/P. This allows to treat systems with large numbers of particles in a reasonable time. Here, N denotes the number of particles and P the number of processors.

	ϵ_{ij} [eV]	σ_{ij} [Å]	$R_{ij}^{(2)}$ [Å]	$R_{ij}^{(3)}$ [Å]	$R_{ij}^{(4)}$ [Å]	$R_{ij}^{(5)}$ [Å]
C–C	4.2038×10^{-3}	3.37	2.0	3.20	9.875	10.0
H–H	5.8901×10^{-3}	2.91	1.7	2.76	9.875	10.0
C–H	4.9760×10^{-3}	3.14	1.8	2.98	9.875	10.0

Table 1
Parameters which are used for the Lennard-Jones van der Waals interaction in addition to the short-ranged Brenner potential [48]. The values for ϵ_{ij}, σ_{ij}, $R_{ij}^{(2)}$, $R_{ij}^{(3)}$ and $R_{ij}^{(5)}$ stem from [55,56]. The parameters ϵ_{CH} and σ_{CH} are given by the Lorentz-Berthelot mixing rules $\epsilon_{\mathrm{CH}} = \sqrt{\epsilon_{\mathrm{CC}}\epsilon_{\mathrm{HH}}}$ and $\sigma_{\mathrm{CH}} = (\sigma_{\mathrm{CC}} + \sigma_{\mathrm{HH}})/2$.

	ϵ_{ij} [eV]	σ_{ij} [Å]	$R_{ij}^{(4)}$ [Å]	$R_{ij}^{(5)}$ [Å]
$\tilde{\mathrm{C}}$–$\tilde{\mathrm{C}}$	6.2040512×10^{-3}	3.9230	9.875	10.0
$\tilde{\mathrm{C}}$–C	5.5562129×10^{-3}	3.6465	9.875	10.0

Table 2
Parameters which are used for the Lennard-Jones van der Waals interaction between the monomeric units $\tilde{\mathrm{C}}$ of the polyethylene and the carbon nanotube atoms C. The parameters $\epsilon_{\tilde{\mathrm{C}}\mathrm{C}}$ and $\sigma_{\tilde{\mathrm{C}}\mathrm{C}}$ are given by the Lorentz-Berthelot mixing rules $\epsilon_{\tilde{\mathrm{C}}\mathrm{C}} = \sqrt{\epsilon_{\tilde{\mathrm{C}}\tilde{\mathrm{C}}}\epsilon_{\mathrm{CC}}}$ and $\sigma_{\tilde{\mathrm{C}}\mathrm{C}} = (\sigma_{\tilde{\mathrm{C}}\tilde{\mathrm{C}}} + \sigma_{\mathrm{CC}})/2$.

United-atom model (Model II)

In our second model, we use a united-atom approach to represent the polyethylene matrix. We employ the so-called expanded collapsed atomic model [50], where the monomeric $\tilde{\mathrm{C}} := \mathrm{CH}_2$ units are treated as single spheres. They interact through a smoothed Lennard-Jones potential

$$V_{LJ}(r_{ij}) = \begin{cases} 4\epsilon_{ij}\left[(\sigma_{ij}/r_{ij})^{12} - (\sigma_{ij}/r_{ij})^{6}\right] & : \quad r_{ij} \le R_{ij}^{(4)} \\ S^{(2)}(r_{ij}) & : \quad R_{ij}^{(4)} \le r_{ij} \le R_{ij}^{(5)} \\ 0 & : \quad r_{ij} \ge R_{ij}^{(5)} \end{cases}$$

between the spheres in different molecules. Within a polyethylene molecule chain, we apply this potential if the spheres are three or more neighbors apart on the chain. In addition to the Lennard-Jones potential, this model includes the usual bond stretching, bond angle bending and torsional potentials. The detailed expressions and the parameters are given in [50]. The carbon nanotube is modeled as before using Brenner's potential. To model the interaction between the spheres of the polyethylene and the carbon atoms of the nanotube, we employ the Lennard-Jones potential with parameters given by the Lorentz-Berthelot mixing rules; see table 2. Note that both the united-atom approach for the polyethylene and the atomistic model for the carbon nanotube can be implemented using the linked cell technique. Furthermore, the

domain decomposition approach can be employed for the parallelization. This again results in a parallel complexity which scales linearly with N/P.

2.3 Elastic moduli and constants

The *stress-strain* relationship provides the overall mechanical response of a material when subjected to mechanical loading under certain conditions. One method to generate *stress-strain* curves is to vary the strain and to measure the stress in the framework of an NVE ensemble [30–32]. Alternatively, we employ our NPT ensemble approach to apply external stress and to measure the corresponding strain. For this purpose, we use an additional external stress tensor Π_{ext} within the equation of motion (5)

$$\dot{p}_h = \left(\Pi_{\text{int}} - \text{diag}\left(P_{\text{ext}}\right) + \Pi_{\text{ext}}\right) h^{-T} \det h - \frac{p_\gamma}{M_T} p_h \,. \tag{11}$$

This way, we are able to accomplish various tensile and compressive load cases to study the elastic properties of a nanotube-polyethylene composite. To generate a stress-strain curve for a tensile or compressive load at given temperature and pressure, we first equilibrate the system with no external stress applied. We then increase or decrease the external stress over a period of time and measure the induced stress $\pi := -\Pi_{\text{int}}$ and the induced strain. To determine the strain, we can express the instantaneous cell matrix $h = (1+e)h_{\text{equi}}$ in terms of the unique displacement matrix e and the equilibrated cell matrix h_{equi}. With the displacement defined as $\vec{u}(\vec{v}) = e\vec{v}$, the linear strain tensor ε is given as

$$\varepsilon_{\alpha\beta} = \frac{1}{2}\left(\frac{\partial u_\alpha}{\partial \vec{v}_\beta} + \frac{\partial u_\beta}{\partial \vec{v}_\alpha}\right) ,$$

which in particular equals the symmetric part $\frac{1}{2}\left(e^T + e\right)$ of the displacement matrix $e = hh_{\text{equi}}^{-1} - 1$. The skew-symmetric part corresponds to the so-called *linear rotational strain tensor*. Because the rotations of the unit cell do not convey any physical meaning, only six (instead of nine; see section 2.1) degrees of freedom are required to control pressure within an NPT ensemble. Therefore, we constrain the 3×3 matrix $\dot{p}_h$ in the equation of motion (11) to be symmetric and assume a symmetric cell matrix h_{equi}. Then, the linear rotational strain tensor vanishes and the linear strain tensor ε equals the displacement matrix e.

In particular, we want to determine *elastic constants*. To calculate components of the *elasticity tensor*, the so-called *elastic moduli* $C_{\alpha\beta\gamma\delta}$, we use the *generalized Hooke's law* [57]

$$\pi_{\alpha\beta} = \sum_{\gamma\delta} C_{\alpha\beta\gamma\delta}\varepsilon_{\gamma\delta} \,, \quad \alpha, \beta \in \{1, 2, 3\} \,. \tag{12}$$

Here, we assume that $\pi_{\alpha\beta}$ are homogeneous linear functions of $\varepsilon_{\gamma\delta}$ and vice versa and that C is a positive-definite fourth order tensor which has *major symmetry* $C_{\alpha\beta\gamma\delta} = C_{\gamma\delta\alpha\beta}$ [58]. For most solid materials such relations hold until the stress reaches the so-called *proportional limit*. If the stresses exceed this limit, the deformation becomes nonlinear but the elastic behavior of the material continues until the stresses reach the so-called *elastic limit*. The general fourth-order tensor C has $3^4 = 81$ independent constants $C_{\alpha\beta\gamma\delta}$. But since π and ε are symmetric second order tensors, the number of independent elastic moduli reduces to $6 \times 6 = 36$. Because of major symmetry it further reduces to $6(6+1)/2 = 21$. Then, we can write the stress-strain relation (12) in matrix form

$$\begin{pmatrix} \pi_{11} \\ \pi_{22} \\ \pi_{33} \\ \pi_{12} \\ \pi_{13} \\ \pi_{23} \end{pmatrix} = \begin{pmatrix} C_{1111} & C_{1122} & C_{1133} & C_{1112} & C_{1113} & C_{1123} \\ C_{1122} & C_{2222} & C_{2233} & C_{2212} & C_{2213} & C_{2223} \\ C_{1133} & C_{2233} & C_{3333} & C_{3312} & C_{3313} & C_{3323} \\ C_{1112} & C_{2212} & C_{3312} & C_{1212} & C_{1213} & C_{1223} \\ C_{1113} & C_{2213} & C_{3313} & C_{1213} & C_{1313} & C_{1323} \\ C_{1123} & C_{2223} & C_{3323} & C_{1323} & C_{1323} & C_{2323} \end{pmatrix} \begin{pmatrix} \varepsilon_{11} \\ \varepsilon_{22} \\ \varepsilon_{33} \\ 2\varepsilon_{12} \\ 2\varepsilon_{13} \\ 2\varepsilon_{23} \end{pmatrix} . \tag{13}$$

We can invert the stress-strain relations (13) by inverting the symmetric 6×6 elastic constant matrix C. This results in

$$\begin{pmatrix} \varepsilon_{11} \\ \varepsilon_{22} \\ \varepsilon_{33} \\ 2\varepsilon_{12} \\ 2\varepsilon_{13} \\ 2\varepsilon_{23} \end{pmatrix} = \begin{pmatrix} S_{1111} & S_{1122} & S_{1133} & S_{1112} & S_{1113} & S_{1123} \\ S_{1122} & S_{2222} & S_{2233} & S_{2212} & S_{2213} & S_{2223} \\ S_{1133} & S_{2233} & S_{3333} & S_{3312} & S_{3313} & S_{3323} \\ S_{1112} & S_{2212} & S_{3312} & S_{1212} & S_{1213} & S_{1223} \\ S_{1113} & S_{2213} & S_{3313} & S_{1213} & S_{1313} & S_{1323} \\ S_{1123} & S_{2223} & S_{3323} & S_{1323} & S_{1323} & S_{2323} \end{pmatrix} \begin{pmatrix} \pi_{11} \\ \pi_{22} \\ \pi_{33} \\ \pi_{12} \\ \pi_{13} \\ \pi_{23} \end{pmatrix} ,$$

where S is the so-called *compliance* matrix. Suppose now that only one of the six independent components of the induced stress is nonzero, say $\pi_{\alpha\beta}$. Then the components

$$\begin{aligned} S_{11\alpha\beta} &= \tfrac{\varepsilon_{11}}{\pi_{\alpha\beta}} , \quad & S_{22\alpha\beta} &= \tfrac{\varepsilon_{22}}{\pi_{\alpha\beta}} , \quad & S_{33\alpha\beta} &= \tfrac{\varepsilon_{33}}{\pi_{\alpha\beta}} , \\ S_{12\alpha\beta} &= \tfrac{2\varepsilon_{12}}{\pi_{\alpha\beta}} , \quad & S_{13\alpha\beta} &= \tfrac{2\varepsilon_{13}}{\pi_{\alpha\beta}} , \quad & S_{23\alpha\beta} &= \tfrac{2\varepsilon_{23}}{\pi_{\alpha\beta}} , \end{aligned}$$

can be determined by calculating the slopes of the corresponding stress-strain curves. Here, the slopes can be easily computed by *least squares linear regression* [59]. This way, we can successively determine the components $S_{\alpha\beta\gamma\delta}$ and consequently the elastic moduli $C_{\alpha\beta\gamma\delta}$.

There is a special elastic constant, the so-called *Young modulus* E. If the stretching force is only applied in uniaxial direction, for example in longitudinal direction, the constant $E_{ll} := \pi_{ll}/\varepsilon_{ll} = 1/S_{llll}$ represents the ratio of the longitudinal stress to the corresponding longitudinal strain. In other words, it is the slope of the stress-strain curve under uniaxial tension. Furthermore, the ratio of transverse contraction strain to longitudinal extension strain in the direction of the stretching force is known as the *Poisson ratio* $\nu := -\varepsilon_{tt}/\varepsilon_{ll}$. Here, tensile deformation is considered positive and compressive deformation is considered negative. Thus, normal materials have a positive ratio. Furthermore, the generalized versions of the Poisson ratio are given by $\nu_{tt,ll} := -S_{ttll}/S_{llll}$.

3 Numerical Experiments

We have extended our existing molecular dynamics package, a load-balanced distributed memory parallel code [51], by the computational methods described in section 2 and conducted several experiments. Here, we run simulations on our PC cluster Parnass2 [60]. It consists of 128 Intel Pentium II 400 MHz processors connected by a 1.28 GBit/s switched Myrinet.

All tensile tests are carried out at *normal conditions*, i.e. for a temperature of 273.15 K and for an external pressure of $1.01325 \cdot 10^{-4}$ GPa. We equilibrate the reference systems in two subsequent steps. First, we use an energy minimization that employs a conjugate-gradient method in order to relax the system to its local potential energy minimum. Then, we conduct a molecular dynamics simulation for 50.0 ps under normal conditions with no external stress applied. Here, we use a timestep of 0.1 fs in the framework of model I and 0.2 fs in the framework of model II. The fictitious mass M_T for the thermostat is set to $10.0\,\mathrm{u\,\AA}^2$ and the fictitious mass M_P for the barostat is set to 10.0 u. In particular, we start the equilibration process with a diagonal cell matrix and allow axial variation only. We study the following systems:

(a) A polyethylene matrix, containing nine chains of 1330 CH_2 units. The equilibrated polyethylene matrix has a density of approximately $0.9\,\mathrm{g/cm^3}$.
(b) A 6 nm capped $(10, 10)$ carbon nanotube embedded in eight chains of 1420 CH_2 units. Each of the carbon nanotube caps consists of one half C_{240} molecule. This way, there are 1020 carbon atoms of the nanotube within the unit cell.
(c) A periodically replicated $(10, 10)$ carbon nanotube spanning the length of the unit cell which is embedded in eight chains of 1095 CH_2 units. There are 1720 carbon atoms of the nanotube within this unit cell.

The original structures for these three systems were made by S. J. V. Frankland, while working with D. W. Brenner and S. P. Adiga. Because the nan-

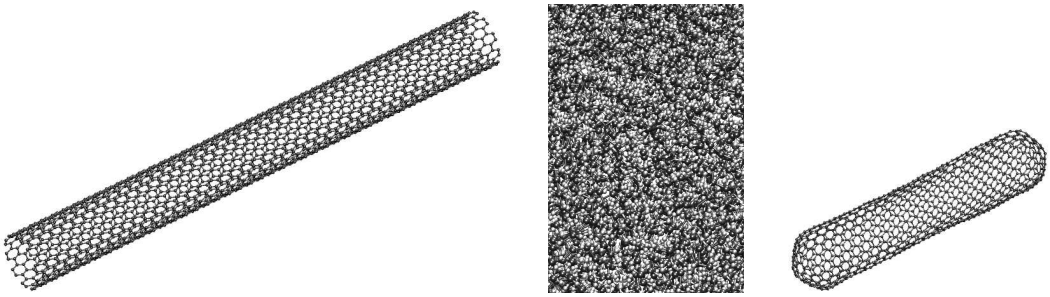

Fig. 1. The nanotubes and the matrix. *Left*: View of the continuous carbon nanotube. *Center*: View into the polyethylene matrix represented by model I. *Right*: View of the capped carbon nanotube.

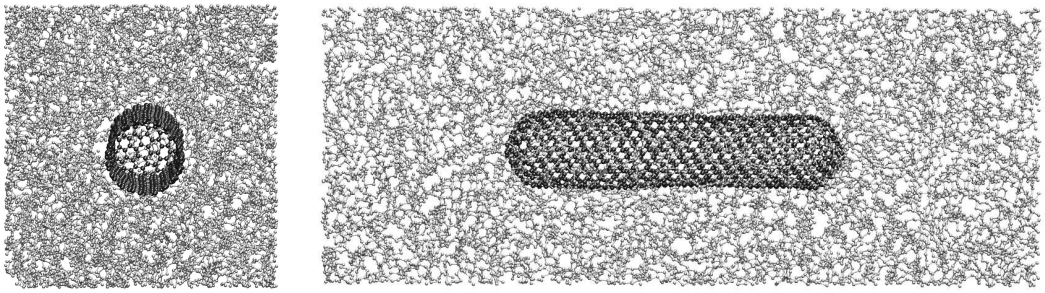

Fig. 2. The unit cell of system (b) represented by model II. *Left*: View into the finite tube within the unit cell. *Right*: Side view of the unit cell.

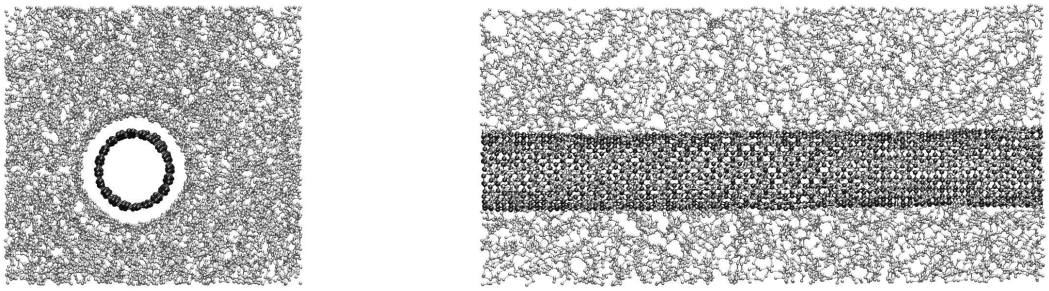

Fig. 3. The unit cell of system (c) represented by model II. *Left*: Front view of unit cell. *Right*: Side view of the unit cell.

otubes are placed along the third axis, systems (b) and (c) are unidirectional composites; see figures 2 and 3. Therefore, we can assume that all considered systems are *orthotropic*. Then, the compliance matrix has only nine independent constants

$$\begin{pmatrix} S_{1111} & S_{1122} & S_{1133} & 0.0 & 0.0 & 0.0 \\ & S_{2222} & S_{2233} & 0.0 & 0.0 & 0.0 \\ & & S_{3333} & 0.0 & 0.0 & 0.0 \\ & & & S_{1212} & 0.0 & 0.0 \\ & & \text{sym} & & S_{1313} & 0.0 \\ & & & & & S_{2323} \end{pmatrix},$$

because the basis vectors lie in the symmetry planes. Details of the equilibrated reference systems are given in table 3.

To study the elastic properties of the polyethylene matrix, we apply a tensile

load for each of the six independent stress components. For that purpose, we employed model I and used a stress rate of 0.01 GPa/ps to increase external stress for the considered component. The resulting compliance matrix can be written in the form

$$\begin{pmatrix} 0.91 & -0.40 & -0.52 & 0.0 & 0.0 & 0.0 \\ & 0.94 & -0.53 & 0.0 & 0.0 & 0.0 \\ & & 1.18 & 0.0 & 0.0 & 0.0 \\ & & & 2.99 & 0.0 & 0.0 \\ & \text{sym} & & & 4.38 & 0.0 \\ & & & & & 3.79 \end{pmatrix} = \frac{1}{E_{33}^{\text{a,II}}} \begin{pmatrix} 0.77 & -0.34 & -0.44 & 0.0 & 0.0 & 0.0 \\ & 0.80 & -0.45 & 0.0 & 0.0 & 0.0 \\ & & 1.00 & 0.0 & 0.0 & 0.0 \\ & & & 2.54 & 0.0 & 0.0 \\ & \text{sym} & & & 3.71 & 0.0 \\ & & & & & 3.22 \end{pmatrix} . \quad (14)$$

Here and in the following, the upper indices denote the system and the model, respectively. If we look at the right hand side of equation (14), we see that the compliance matrix of system (a) has nearly isotropic form

$$\frac{1}{\tilde{E}} \begin{pmatrix} 1 & -\tilde{\nu} & -\tilde{\nu} & 0.0 & 0.0 & 0.0 \\ & 1 & -\tilde{\nu} & 0.0 & 0.0 & 0.0 \\ & & 1 & 0.0 & 0.0 & 0.0 \\ & & & 2(1+\tilde{\nu}) & 0.0 & .0.0 \\ & \text{sym} & & & 2(1+\tilde{\nu}) & 0.0 \\ & & & & & 2(1+\tilde{\nu}) \end{pmatrix} = 1.18 \begin{pmatrix} 0.77 & -0.44 & -0.44 & 0.0 & 0.0 & 0.0 \\ & 0.80 & -0.44 & 0.0 & 0.0 & 0.0 \\ & & 1.00 & 0.0 & 0.0 & 0.0 \\ & & & 2.89 & 0.0 & .0.0 \\ & \text{sym} & & & 2.89 & 0.0 \\ & & & & & 2.89 \end{pmatrix} ,$$

with Young modulus $\tilde{E} := E_{33}^{\text{a,II}} \approx 0.85$ and Poisson ratio $\tilde{\nu} := (\nu_{11,33}^{\text{a,II}} + \nu_{22,33}^{\text{a,II}})/2 \approx 0.44$; see table 5. Then, we used model II to perform the same tensile tests to compute the compliance matrix of system (b) and (c); see table 4. Additionally, we calculated the elastic constant matrix by inverting the compliance matrix. Furthermore, we used model I to apply uniaxial external stress to system (a), (b) and (c) to determine the Young moduli and the Poisson ratios for the third coordinate direction. Additionally, we computed the Young moduli corresponding to loading in the direction of the first coordinate. The results are summarized in table 5. The compliance and elasticity tensors in table 4 and the elastic constants in table 5 show the anisotropic behavior of the systems (b) and (c). In the same way, we determined the Young modulus and the Poisson ratio of the periodically replicated $(10, 10)$ carbon nanotube of system (c) without the polyethylene matrix. For the modulus, which corresponds to a tensile load in the direction of the axis of the nanotube, we obtained 403.85 GPa. For the associated Poisson ratio a value of 0.23 resulted. Here, we assumed the carbon nanotube as a hollow cylinder with thickness 3.4 Å to calculate the volume [23]. This way, we obtained an equilibrated volume of 16.075 nm^3. Note that there is a lot of variance among the elastic moduli reported by several groups [61]. For example, ≈ 300 GPa [62], ≈ 600 GPa [22] and ≈ 1 TPa [23] are given for the uniaxial Young modulus of a $(10, 10)$ carbon nanotube in the literature. For this nanotube, the Poisson ratio is noted as 2.5 [20], 2.78 [23] and 2.87 [62], respectively. The application of different approaches, models and parameters is likely to be responsible for this variety of results. Additionally, if we apply the Langrange strain tensor [57,58], we get a Young modulus of 395.04 GPa and a Poisson ratio of 0.22. If we apply the logarithmic strain tensor [57,58], we get a Young modulus of 410.18 GPa and a Poisson ratio of 0.24.

System	Model	h_{equi} [Å]	Ω_{equi} [nm^3]
(a)	I	diag (49.13, 48.41, 130.86)	311.23
(a)	II	diag (50.37, 47.90, 130.16)	314.04
(b)	I	diag (51.35, 51.57, 129.36)	342.56
(b)	II	diag (49.92, 52.20, 131.70)	343.19
(c)	I	diag (47.84, 48.50, 105.43)	244.62
(c)	II	diag (48.30, 48.22, 106.81)	248.76

Table 3
Reference cell matrices and cell volumes of the studied systems for model I and II. In particular, the volume fraction of the carbon nanotube is approximately 2.8% for system (b), and approximately 6.5% for system (c).

System	S	C
(b)	$\begin{pmatrix} 1.24 & -0.62 & -0.21 & 0.0 & 0.0 & 0.0 \\ & 1.27 & -0.18 & 0.0 & 0.0 & 0.0 \\ & & 0.57 & 0.0 & 0.0 & 0.0 \\ & & & 3.43 & 0.0 & 0.0 \\ & \text{sym} & & & 5.27 & 0.0 \\ & & & & & 5.88 \end{pmatrix}$	$\begin{pmatrix} 1.29 & 0.73 & 0.71 & 0.0 & 0.0 & 0.0 \\ & 1.24 & 0.67 & 0.0 & 0.0 & 0.0 \\ & & 2.22 & 0.0 & 0.0 & 0.0 \\ & & & 0.29 & 0.0 & 0.0 \\ & \text{sym} & & & 0.19 & 0.0 \\ & & & & & 0.17 \end{pmatrix}$
(c)	$\begin{pmatrix} 1.013 & -0.351 & -0.0087 & 0.0 & 0.0 & 0.0 \\ & 0.869 & -0.0085 & 0.0 & 0.0 & 0.0 \\ & & 0.0393 & 0.0 & 0.0 & 0.0 \\ & & & 2.83 & 0.0 & 0.0 \\ & \text{sym} & & & 7.47 & 0.0 \\ & & & & & 5.94 \end{pmatrix}$	$\begin{pmatrix} 1.14 & 0.44 & 0.35 & 0.0 & 0.0 & 0.0 \\ & 1.32 & 0.38 & 0.0 & 0.0 & 0.0 \\ & & 25.59 & 0.0 & 0.0 & 0.0 \\ & & & 0.35 & 0.0 & 0.0 \\ & \text{sym} & & & 0.13 & 0.0 \\ & & & & & 0.17 \end{pmatrix}$

Table 4
The compliance matrix S and the elastic constant matrix C for systems (b) and (c) for model II.

System	Model	E_{33}[GPa]	$\nu_{11,33}$	$\nu_{22,33}$	E_{11}[GPa]
(a)	I	0.6142	0.4850	0.4304	0.7100
(a)	II	0.8495	0.4394	0.4501	1.1034
(b)	I	1.4777	0.2778	0.3532	0.6455
(b)	II	1.7422	0.3722	0.3215	0.8043
(c)	I	23.395	0.2161	0.2795	1.1010
(c)	II	25.435	0.2222	0.2157	0.9868

Table 5
Elastic moduli and Poisson ratios of the studied systems for model I and model II. The longitudinal moduli are increasing and the transversal are constant. The Poisson ratios are decreasing to the ratio of the $(10, 10)$ carbon nanotube.

In particular, all simulations were conducted under normal conditions. Here, the same timesteps and fictitious masses as in the molecular dynamics part of the equilibration process were used. Furthermore, a stress rate of 0.01 GPa/ps was taken in all tensile load test cases. A molecular dynamics tensile simulation was stopped when a strain of 10 % was reached.

4 Discussion

From the results of table 5 we see the following: Subjected to *transverse* loading conditions, the Young modulus of the composite is in the range of the modulus of the matrix. Thus, there is no reinforcement of the matrix. Subjected to *longitudinal* loading conditions, we see a Young modulus two times higher for system (b) and a Young modulus approximately thirty times higher for system (c).

For a nanocomposite under uniaxial loading, the dependence of the elastic modulus on the nanotube volume fraction can be estimated by the macroscopic rule-of-mixtures. This rule reads as

$$E_c = \Omega_f E_f + (1 - \Omega_f) E_m \,, \tag{15}$$

where E_c denotes the predicted Young modulus of the composite, E_f denotes the Young modulus of the fiber, E_m denotes the Young modulus of the matrix and Ω_f denotes the volume fraction of the fiber.

Let us consider system (c) first. The modulus of a $(10, 10)$ carbon nanotube was $E_f = 403.85\,\mathrm{GPa}$ and its volume fraction was 6.5 %; see section 3 and table 3. If we now use $E_m = E_{33}^{a,I} = 0.61\,\mathrm{GPa}$ for the modulus of the matrix, the rule-of-mixtures gives a prediction of $E_c \approx 26.82\,\mathrm{GPa}$ for the modulus of the composite in the case of model I. In an analogous way, the rule-of-mixtures gives an estimated modulus for model II of $E_c \approx 27.04\,\mathrm{GPa}$. These values are in the range of our measured moduli $E_{33}^{c,I} = 23.39\,\mathrm{GPa}$ and $E_{33}^{c,II} = 25.43\,\mathrm{GPa}$ for system (c) in table 5.

Now we consider system (b). With a volume fraction of 2.8 %, the rule-of-mixtures predicts a modulus of $E_c \approx 12\,\mathrm{GPa}$, which is substantially larger than the results of our measurements; see table 5. But we can expect this lack of effect, because the 6 nm carbon nanotube is too short compared with the size of the unit cell of the composite. In particular, a typical single-walled carbon nanotube is approximately 250 times longer. To overcome this finite size effect, we follow Liu and Chen [28,29] and employ an extended rule-of-mixtures

$$E_c^{\mathrm{ex}} = \left(\frac{1}{E_m} \frac{(L - L_c)}{L} + \frac{1}{E_c} \frac{L_c}{L} \frac{A}{A_c} \right)^{-1} , \tag{16}$$

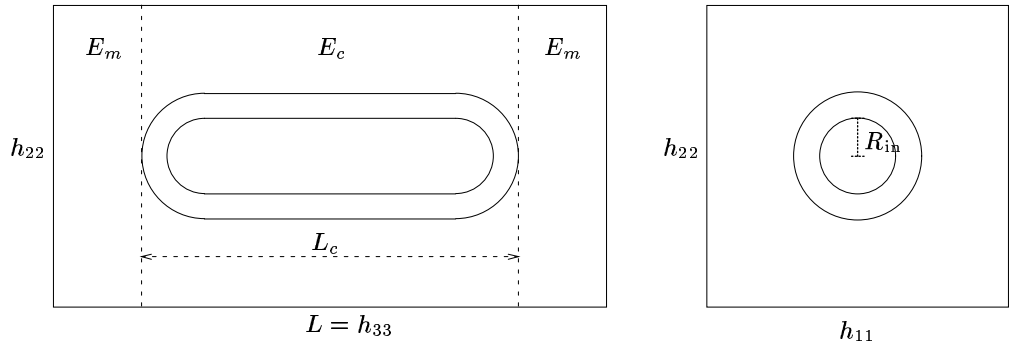

Fig. 4. Schematic diagram of the unit cell of system (b). Here, we define the areas $A = h_{11}h_{22}$ and $A_c = A - \pi R_{\text{in}}^2$. Furthermore, we assume $L_c = 6\,\text{nm}$ and $R_{\text{in}} = 5\,\text{nm}$.

which also takes the distribution of the fiber into account, contrary to equation (15); see figure 4. This extended rule-of-mixtures gives a prediction of $E_c^{\text{ex}} \approx 1.11\,\text{GPa}$ for the modulus of the composite in the case of model I and a prediction of $E_c^{\text{ex}} \approx 1.52\,\text{GPa}$ for model II. These values are in the range of our measured moduli $E_{33}^{b,I} = 1.47\,\text{GPa}$ and $E_{33}^{b,II} = 1.74\,\text{GPa}$; see table 5. Here, we applied equation (15) in combination with a volume fraction of 6 % to estimate the modulus $E_c \approx 24.81\,\text{GPa}$ for model I and the modulus $E_c \approx 25.03\,\text{GPa}$ in the case of model II. The remaining values which we used to employ equation (16), are given in figure 4, table 3, and table 5.

Furthermore, there is only a slight difference between model I and model II, because no forming or breaking of bonds takes place in the equilibration processes and tensile simulations, we performed. In particular, if we use the *reactive* model I for system (a) or for system (b), we observe no forming of chemical bonds between the polyethylene matrix and the nanotube which would strengthen the interfacial adhesion [31]. Therefore, we anticipate that a longer and a functionalized nanotube [30,31] would lead to improved reinforcement. Especially in the case of functionalized carbon nanotubes, the second-generation REBO potential [63] can be used to model the hydrocarbon system with enhanced accuracy.

5 Concluding Remarks

The results of a molecular dynamics simulation study for the analysis of elastic properties of a *carbon nanotube/polyethylene composite* was presented. Here, we used the Parrinello-Rahman technique to apply external stress to generate stress-strain curves. As model problems we considered a short and an infinite carbon nanotube which were embedded into a polyethylene matrix. Load was applied to calculate the compliance matrix and different elastic constants like the Young modulus and the Poisson ratio. We used two different ways to model these systems: first Brenner's potential only, and second Brenner's potential for

the nanotube but a united-atom potential for the polyethylene matrix. Here, these two different models show nearly the same results, because there are no chemical bonds between the fiber and the matrix. Furthermore, the calculated Young moduli were compared to two different rule-of-mixtures. The simple rule, which takes only the volume fraction of the fiber into account, holds for the long continuous nanotube, and the extended rule, which also takes the distribution of the fiber into account, holds for the short fully embedded nanotube.

The simulation results suggest the possibility to use nanotubes to reinforce an appropriate matrix. They furthermore indicate that long nanotubes should be used. For a fixed tensile loading direction, the nanotubes should be aligned parallel with the loading direction. For general kinds of loading directions, very long nanotubes in random orientation will most likely produce the best results.

6 Acknowledgments

This work is based in parts on the results of a collaboration with S. J. V. Frankland, A. Caglar and D. W. Brenner. It was supported by a grant from the *Sonderforschungsbereich 408* of the *Deutsche Forschungsgemeinschaft*. Furthermore, we thank M. Arndt, L. Jager and R. Wildenhues, who were involved in the development of our molecular dynamics software package.

References

[1] H. W. Kroto, J. R. Heath, S. C. O'Brien, R. F. Curl, R. E. Smalley, C_{60} buckminsterfullerene, Nature 318 (1985) 162–163.

[2] S. Iijima, Helical microtubules of graphitic carbon, Nature 354 (1991) 56–58.

[3] R. E. Smalley, D. T. Colbert, Self assembly of fullerene tubes and balls, talk to: Robert A. Welch Foundation (October 1995).

[4] M. M. J. Treacy, T. W. Ebbesen, J. M. Gibson, Exceptionally high Young's modulus observed for individual carbon nanotubes, Nature 381 (1996) 678–680.

[5] B. I. Yakobson, R. E. Smalley, Fullerene nanotubes: $C_{1,000,000}$ and beyond, American Scientist 85 (4) (1997) 324–337.

[6] P. M. Ajayan, L. S. Schadler, S. C. Giannaris, A. Rubio, Single-walled carbon nanotube-polymer composites: Strength and weakness, Adv. Materials 12 (2000) 750–753.

[7] C. Bower, R. Rosen, L. Jin, J. Han, O. Zhou, Deformation of carbon nanotubes in nanotube-polymer composites, Appl. Phys. Lett. 74 (1999) 3317–3319.

[8] M. L. de la Chapelle, C. Stephan, T. P. Nguyen, S. Lefrant, C. Journet, P. Bernier, E. Munoz, A. Benito, W. K. Maser, M. T. Martinez, G. D. de la Fuente, T. Guillard, G. Flamant, L. Alvarez, D. Laplaze, Raman characterization of singlewalled carbon nanotubes and PMMA-nanotubes composites, Synthetic Metals 103 (1999) 2510–2512.

[9] X. Gong, J. Liu, S. Baskaran, R. D. Voise, J. S. Young, Surfactant-assisted processing of carbon nanotube/polymer composite, Chem. Mater. 12 (2000) 1049–1052.

[10] R. Haggemueller, H. H. Gommas, A. Rinzler, J. E. Fischer, K. I. Winey, Aligned single-wall carbon nanotubes in composites by melt processing methods, Chem. Phys. Lett. 330 (2000) 219–225.

[11] Z. Jia, Z. Wang, C. Xu, J. Liang, B. Wei, D. Wu, S. Zhu, Study on poly(methylmethacrylate)/carbon nanotube composites, Mat. Sci. Eng. A 271 (1999) 395–400.

[12] L. Jin, C. Bower, O. Zhou, Alignment of carbon nanotubes in a polymer matrix by mechanical stretching, Appl. Phys. Lett. 73 (1998) 1197–1199.

[13] D. Qian, E. C. Dickey, R. Andrews, T. Rantell, Load transfer and deformation mechanisms in carbon nanotube-polystyrene composites, Appl. Phys. Lett. 76 (2000) 2868–2870.

[14] M. S. P. Schaffer, A. H. Windle, Fabrication and characterization of carbon nanotube/poly(vinyl alcohol) composites, Adv. Materials 11 (1999) 937–941.

[15] L. S. Schadler, S. C. Giannaris, P. M. Ajayan, Load transfer in carbon nanotube epoxy composites, Appl. Phys. Lett. 73 (1998) 3842–3844.

[16] D. H. Robertson, D. W. Brenner, J. W. Mintmire, Energetics of nanoscale graphitic tubules, Phys. Rev. B 45 (21) (1992) 12592–12595.

[17] M. B. Nardelli, B. I. Yakobson, J. Bernholc, Mechanism of strain release in carbon nanotubes, Phys. Rev. B 57 (8) (1998) R4277–R4280.

[18] S. Reich, C. Thomsen, P. Ordejón, Elastic properties of carbon nanotubes under hydrostatic pressure, Phys. Rev. B 65 (2002) 153407.

[19] J. Hamaekers, Ebene-Wellen basiertes, adaptives und paralleles Verfahren für die Dichtefunktionaltheorie, Diplomarbeit, Institut für Angewandte Mathematik, Universität Bonn, Germany (2002).

[20] E. Hernández, C. Goze, P. Bernier, A. Rubio, Elastic properties of C and $B_xC_yN_z$ composite nanotubes, Phys. Rev. Lett. 80 (20) (1998) 4502–4505.

[21] B. I. Yakobson, C. J. Brabec, J. Bernholc, Nanomechanics of carbon tubes: Instabilities beyond linear response, Phys. Rev. Lett. 76 (14) (1996) 2511–2514.

[22] C. F. Cornwell, L. T. Wille, Elastic properties of single-walled carbon nanotubes in compression, Solid State Commun. 101 (1997) 555–558.

[23] J. P. Lu, Elastic properties of carbon nanotubes and nanoropes, Phys. Rev. Lett. 79 (7) (1997) 1297–1300.

[24] A. Caglar, M. Griebel, On the numerical simulation of fullerene nanotubes: $C_{100.000.000}$ and beyond!, in: R. Esser, P. Grassberger, J. Grotendorst, M. Lewerenz (Eds.), Molecular Dynamics on Parallel Computers, NIC, Jülich 8-10 February 1999, World Scientific, 2000.

[25] D. Qian, W. K. Liu, R. S. Ruoff, Mechanics of C_{60} in nanotubes, J. Phys. Chem. B 105 (2001) 10753–10758.

[26] T. Belytschko, S. P. Xiao, C. Schatz, R. S. Ruoff, Atomistic simulations of nanotube fracture, Phys. Rev. B 65 (2002) 235430.

[27] B. Ni, S. B. Sinnott, P. T. Mikulski, J. A. Harrison, Compression of carbon nanotubes filled with C_{60}, CH_4, or Ne: Predictions from molecular dynamics simulations, Phys. Rev. Lett. 88 (20) (2002) 205505.

[28] Y. J. Liu, X. L. Chen, Evaluations of the effective material properties of carbon nanotube-based comopsites using a nanoscale representative volume element, Mechanics of Materials 35 (2003) 69–81.

[29] X. Chen, Y. J. Liu, Square representative volume elements for evaluating the effective material properties of carbon nanotube-based composites, Computational Materials Science 29 (1) (2004) 1–11.

[30] S. J. V. Frankland, A. Caglar, D. W. Brenner, M. Griebel, Reinforcement mechanisms in polymer nanotube composites: Simulated non-bonded and cross-linked systems, in: Proceedings of the MRS Fall Meeting, 2000.

[31] S. J. V. Frankland, A. Caglar, D. W. Brenner, M. Griebel, Molecular simulation of the influence of chemical cross-links on the shear strength of carbon nanotube-polymer interfaces, J. Phys. Chem. B 106 (2002) 3046–3048.

[32] S. J. V. Frankland, V. M. Harik, G. M. Odegard, D. W. Brenner, T. S. Gates, The stress-strain behavior of polymer-nanotube composites from molecular dynamics simulations, Composites Science and Technology 63 (11) (2003) 1655–1661.

[33] D. N. Theodorou, U. W. Suter, Atomistic modeling of mechanical properties of polymeric glasses, Macromolecules 19 (1986) 139–154.

[34] K. W. Wojciechowski, K. V. Tretiakov, A. C. Brańka, M. Kowalik, Elastic properties of two-dimensional hard disks in the close-packing limit, J. Chem. Phys. 119 (2) (2003) 939–946.

[35] M. Parrinello, R. Rahman, Crystal structure and pair potentials: A molecular-dynamics study, Phys. Rev. Lett. 45 (14) (1980) 1196–1199.

[36] M. Parrinello, A. Rahman, Strain fluctuations and elastic constants, J. Chem. Phys. 76 (5) (1982) 2662–2666.

[37] J. R. Ray, A. Rahman, Statistical ensembles and molecular dynamics studies of anisotropic solids, J. Chem. Phys. 80 (1984) 4423–4428.

[38] J. R. Ray, A. Rahman, Statistical ensembles and molecular dynamics studies of anisotropic solids. II, J. Chem. Phys. 82 (1985) 4243–4247.

[39] J. R. Ray, Elastic constants and statistical esembles in molecular dynamics, Comp. Phys. Rep. 8 (1988) 109–152.

[40] A. A. Gusev, M. M. Zehnder, U. W. Suter, Fluctuation formula for elastic constants, Phys. Rev. B 54 (1) (1996) 1–4.

[41] M. Karimi, G. Stapay, T. Kaplan, M. Mostoller, Temperature dependence of the elastic constants of Ni: Reliability of EAM in predicting thermal properties, Modelling Simul. Mater. Sci. Eng. 5 (1997) 337–346.

[42] Z. Zhou, Fluctuations and thermodynamics properties of the constant shear strain ensemble, J. Chem. Phys. 114 (20) (2001) 8769–8774.

[43] M. Parrinello, A. Rahman, Polymorphic transitions in single crystals: A new molecular dynamics method, J. Appl. Phys. 52 (12) (1981) 7182–7190.

[44] H. J. C. Berendsen, J. P. M. Postma, W. F. van Gunsteren, A. DiNola, J. R. Haak, Molecular dynamics with coupling to an external bath, J. Chem. Phys. 81 (1984) 3684–3690.

[45] D. Brown, J. H. R. Clarke, Molecular dynamics simulation of an amorphous polymer under tension. 1. Phenomenology, Macromolecules 24 (1991) 2075–2082.

[46] S. Blonski, W. Brostow, J. Kubát, Molecular-dynamics simulations of stress relaxation in metals and polymers, Phys. Rev. B 49 (10) (1994) 6494–6500.

[47] S. Nose, M. L. Klein, Constant pressure molecular dynamics for molecular systems, J. Mol. Phys. 50 (1983) 1055–1076.

[48] D. W. Brenner, Empirical potential for hydrocarbons for use in simulating the chemical vapor deposition of diamond films, Phys. Rev. B 42 (15) (1990) 9458–9471.

[49] D. W. Brenner, Erratum: Empirical potential for hydrocarbons for use in simulating the chemical vapor deposition of diamond films, Phys. Rev. B 46 (3) (1990) 1948.

[50] S. H. Lee, H. Lee, H. Pak, J. C. Rasaiah, Molecular dynamics simulation of liquid alkanes. I. Thermodynamics and structures of normal alkanes: n-butane to n-heptadecane, Bull. Korean Chem. Soc. 17 (1996) 735–744.

[51] M. Griebel, A. Caglar, S. Knapek, G. Zumbusch, Numerische Simulation in der Moleküldynamik. Numerik, Algorithmen, Parallelisierung, Anwendungen, Springer, Berlin, Heidelberg, 2003.

[52] W. Smith, Calculating the pressure, CCP5 Info. Quart. 39 (1993) 14–21.

[53] D. Beeman, Some multistep methods for use in molecular dynamics calculations, J. Comp. Phys. 20 (1976) 130–139.

[54] K. Refson, Molecular dynamics simulation of solid n-butane, Physica B 131 (1985) 256–266.

[55] M. A. Moller, D. J. Tildesley, K. S. Kim, N. Quirke, Molecular dynamics simulation of a Langmuir-Blodgett film, J. Chem. Phys. 94 (1991) 8390–8401.

[56] Z. Mao, A. Garg, S. B. Sinnott, Molecular dynamics simulations of the filling and decorating of carbon nanotubules, Nanotechnology 10 (1999) 273–277.

[57] D. S. Chandrasekharaiah, L. Debnath, Continuum Mechanics, Academic Press, San Diego, 1994, Ch. 9.2.

[58] T. Belytschko, W. K. Liu, B. Moran, Nonlinear Finite Elements for Continua and Structures, John Wiley & Sons, Chichester, 2000, Ch. 5.

[59] W. H. Press, S. A. Teukolsky, W. T. Vetterling, B. P. Flannery, Numerical recipes in C: The art of scientific computing, 2nd Edition, Cambridge University Press, 1992.

[60] http://wissrech.iam.uni-bonn.de/research/projects/parnass2/index.html.

[61] Y. Xia, M. Zhao, Y. Ma, M. Ying, X. Liu, P. Liu, L. Mei, Tensile strength of single-walled carbon nanotubes with defects under hydrostatic pressure, Phys. Rev. B 65 (2002) 155415–1.

[62] G. Dereli, C. Özdoğan, Structural stability and energetics of single-walled carbon nanotubes under uniaxial strain, Phys. Rev. B 67 (2003) 035416–1.

[63] D. W. Brenner, O. A. Shenderova, J. A. Harrison, S. J. Stuart, B. Ni, S. B. Sinnott, A second-generation reactive empirical bond order (REBO) potential energy expression for hydrocarbons, J. Phys.: Condens. Matter 14 (2002) 783–802.